

Dynamics of multiphase turbulent plumes with hybrid buoyancy sources in stratified environments

Alexandre Fabregat Tomàs, Andrew C. Poje, Tamay M. Özgökmen, and William K. Dewar

Citation: *Physics of Fluids* **28**, 095109 (2016); doi: 10.1063/1.4963313

View online: <http://dx.doi.org/10.1063/1.4963313>

View Table of Contents: <http://scitation.aip.org/content/aip/journal/pof2/28/9?ver=pdfcov>

Published by the [AIP Publishing](#)

Articles you may be interested in

[On the scaling of the slip velocity in turbulent flows over superhydrophobic surfaces](#)

Phys. Fluids **28**, 025110 (2016); 10.1063/1.4941769

[Dynamics of rising bubble inside a viscosity-stratified medium](#)

Phys. Fluids **27**, 072105 (2015); 10.1063/1.4927521

[Evidence for Bolgiano-Obukhov scaling in rotating stratified turbulence using high-resolution direct numerical simulations](#)

Phys. Fluids **27**, 055105 (2015); 10.1063/1.4921076

[Experimental and numerical study of buoyancy-driven single bubble dynamics in a vertical Hele-Shaw cell](#)

Phys. Fluids **26**, 123303 (2014); 10.1063/1.4903488

[Stratified turbulence at the buoyancy scale](#)

Phys. Fluids **23**, 066602 (2011); 10.1063/1.3599699



Looking for a specific instrument?

Easy access to the latest equipment.
Shop the *Physics Today* Buyer's Guide.

PHYSICS TODAY

lasers imaging
VACUUM EQUIPMENT instrumentation
software **MATERIALS**
cryogenics + MORE...

Dynamics of multiphase turbulent plumes with hybrid buoyancy sources in stratified environments

Alexandre Fabregat Tomàs,^{1,a)} Andrew C. Poje,¹ Tamay M. Özgökmen,² and William K. Dewar³

¹*Department of Mathematics, City University of New York, College of Staten Island, 2800 Victory Boulevard, Staten Island, New York 10314, USA*

²*Rosenstiel School of Marine and Atmospheric Science, University of Miami, 4600 Rickenbacker Causeway, Miami, Florida 33149-1098, USA*

³*Earth, Ocean and Atmospheric Science, Florida State University, P.O. Box 3064520, Tallahassee, Florida 32306-4520, USA*

(Received 1 June 2016; accepted 10 September 2016; published online 28 September 2016)

Deepwater oil blowouts typically generate multiphase hybrid plumes where the total inlet buoyancy flux is set by the combined presence of gas, oil, and heat. We numerically investigate the effects of combined sources of inlet buoyancy on turbulent plume dynamics by varying the inputs of a dispersed, slipping gas phase and a non-slipping buoyant liquid phase in thermally stratified environments. The ability of a single momentum equation, multiphase model to correctly reproduce characteristic plume heights is validated for both dispersed liquid phase and pure gas bubble plumes. A hybrid case, containing buoyancy contributions from both gas and liquid phases, is also investigated. As expected, on the plume centerline, the presence of a slipping gas phase increases both the vertical location of the neutrally buoyant equilibrium height and the maximum vertical extent of the liquid effluent relative to non-bubble plumes. While producing an overall increase in the plume height, the presence of a slipping gas phase also significantly enhances both the extent and magnitude of negatively buoyant downdrafts in the outer plume region. As a result, the intrusion or trapping height, the vertical distance where liquid phase plume effluent accumulates, is found to be significantly lower in both bubble and hybrid plumes. Below the intrusion level, the simulations are compared to an integral model formulation that explicitly accounts for the effects of the gas slip velocity in the evolution of the buoyancy flux. Discrepancies in the integral model and full solutions are largest in the source vicinity region where vertical turbulent volume fluxes, necessarily neglected in the integral formulation, are significant. *Published by AIP Publishing.* [<http://dx.doi.org/10.1063/1.4963313>]

I. INTRODUCTION

Buoyant plumes are generated by density defects typically produced by gradients of temperature or salinity or by the injection of a lighter secondary phase. Quantifying the mixing properties of plumes is essential in a variety of industrial and geophysical applications. In particular, we are interested in improving our understanding of the turbulent transport of pollutants in the extreme case of deepwater oil blowouts such as the 2010 Deepwater Horizon (DwH) incident.¹ Blowout plumes are distinguished by extremely large inlet buoyancy fluxes and turbulent dynamics complicated by a host of physico-chemical processes associated with both the ambient conditions at the sea floor and the complex multi-phase nature of the hot effluent.² In such plumes, driven by multiple sources of buoyancy at the inlet, determining how much of the effluent reaches the surface and the distribution

^{a)}Email: alex.fabregat@csi.cuny.edu

of pollutant constituents within the water column is of primary importance for remediation and response efforts.

The simplest turbulent plume configuration, a point source of Boussinesq temperature-driven buoyancy anomaly evolving in a uniform environment, was first analyzed by Schmidt³ and Zeldovich.⁴ Using mixing length arguments and self-similar profiles of vertical velocity and temperature, they derived the well-known, experimentally validated, scaling laws governing the vertical decay rates of momentum and buoyancy flux.^{5,6} By relating the turbulent radial volume flux at the plume interface to the characteristic vertical velocity via a simple entrainment coefficient,⁷ Morton *et al.*⁸ derived explicit equations for the vertical evolution of integrated volume, momentum, and buoyancy fluxes for self-similar plumes. Provided with experimentally determined values of a constant entrainment coefficient, integral models have been used to predict mean profiles of fluxes in both uniform and stably stratified environments, in the latter case for the region below the main lateral intrusion level where self-similarity necessarily fails.⁹ The coherent motions in the plume top region, unattainable using integral solutions, have been studied with negatively buoyant fountain models.¹⁰

Integral model approaches have been extended to a variety of more complex situations including multiphase plumes generated by the injection of gas bubbles,^{11–13} buoyancy-reversing volcanic plumes,^{14,15} or plumes with chemical reactions.¹⁶ In the bubble plume case, the gas phase is characterized by an additional velocity scale, namely, the slip velocity of the bubbles relative to the liquid phase.¹⁷ The distinct dynamics of bubble plumes are typically modeled adding two additional experimental parameters to the momentum flux equation: the momentum amplification factor modeling the increase in turbulence in the presence of bubbles and the non-unitary ratio of bubble to momentum plume widths due to the slip.^{18–21}

Under stratification, a single phase plume grows in the vertical driven by the buoyancy flux as it entrains fluid from the surroundings. Eventually the plume reaches the neutral buoyancy level but continues to grow due to inertial effects transitioning into a fountain where the “too dense” fluid detrains and falls back generating an outer ring of downdrafts. The single phase plume therefore is constrained below this maximum height and the constant inflow at the inlet is balanced by the horizontal transport across the intrusion. In contrast, buoyancy carried by gas bubbles constantly escapes from the carrier phase, eventually destratifying the entire water column within the plume region. Primary differences with respect to the single phase case occur in the inertial overshoot region where the carrier fluid is locally too dense and falls or “peels” from the bubble plume forming the intrusion level. Above the primary trapping height, the process may repeat creating secondary intrusions as shown in the experiments^{17,22} that were also used to analyze the dependence of the overall plume topology on the slip velocity. For moderate values of the slip velocity, the results suggest that while the peeling height increases as the bubbles slip faster, the trapping height dependency is weak. The results, however, are characterized by a large amount of scatter.²³ On the modelling side, double plume approaches have been proposed to extend the concepts of the integral model to bubble plumes in stratified environments.^{17,24–26} The bubble plume is typically decomposed into an upward bubbly core and an outer ring of downdrafts that represents the detraining (“peeling”) fluid. Solutions are only obtained after estimating entrainment fluxes between these idealized regions and the quiescent environment.

The goal in this paper is to use turbulence resolving numerical simulations to analyze the turbulent mixing of multiphase plumes in an effort to advance modelling and parameterization of more realistic deepwater blowouts containing multiple buoyancy sources at the well-head. While gas bubble plumes have been the focus of a considerable amount of theoretical and experimental effort both in uniform^{13,18,21,27,28} and stratified environments,^{17,22–26,29–32} less attention has been given to the dynamics of hybrid bubble plumes driven by the combined effects of a mixture of inlet gas and buoyant liquid. To this end, in addition to the gas phase, we also consider a discrete, non-slipping secondary liquid phase lighter than the ambient fluid. We take the liberty of referring to this dispersed, non-slipping secondary liquid phase, very loosely, as “oil.” Compared to a single-phase case where local density may depend, for instance, on both salinity and temperature, the two-liquid system is differentiated by the differences in the thermodynamic properties of the phases retained in mixture equation of state. When the two fluids are distinguished only by modest differences in

density through (here temperature independent) thermal expansion coefficients, the effects of the resulting quadratic non-linearity are found to be minimal. Under the highly idealized assumption that there is no relative motion between the liquid phases, releasing “oil” in the present formulation is therefore equivalent to releasing fresh water into a uniformly saline, thermally stratified brine.

Here we fix the total buoyancy flux and quantify the changes in characteristic plume heights and turbulent mixing produced by varying the fractional contributions of gas and liquid buoyancy sources. The cases studied include plumes produced by injecting only gas bubbles, only a lighter liquid phase and a hybrid case involving both buoyancy components. The plumes evolve in a thermally stratified environment with constant temperature gradient. Section II describes the single momentum equation multiphase model used and also provides a derivation of the corresponding integral model, explicitly accounting for the gas slip velocity. Section III presents the numerical experiments conducted along with details on the boundary conditions and the numerical solver used to solve the model equations. Results are presented in Section IV which includes a validation of the simplified multiphase model against isothermal bubble plume experiments and comparisons between the full simulations and the derived integral model. Conclusions are presented in Section V.

II. MODEL EQUATIONS

A. Gas-bubble plume model

For computational purposes, we consider a standard Eulerian-Eulerian, Boussinesq model for multiphase plumes. As explained in detail in the work of Fabregat *et al.*,²⁰ the main assumptions in the current model are as follows: (i) Boussinesq conditions (density variations appear only in the buoyancy term), (ii) bubbles carry a negligible amount of momentum compared to the liquid phase,³³ and (iii) the slip velocity of the gas phase is constant.^{33,34} The Boussinesq assumption constrains the model to dilute bubble plumes with small gas volume fractions.

The mass conservation equation for a phase k can be written as

$$\frac{\partial}{\partial \tilde{t}} (\alpha_k \rho_k) + \nabla \cdot (\alpha_k \rho_k \tilde{\mathbf{u}}_k) = 0, \quad (1)$$

where \tilde{t} is time and ρ_k , α_k , and $\tilde{\mathbf{u}}_k = (\tilde{u}, \tilde{v}, \tilde{w})_k$ are density, volume fraction, and Cartesian velocity field for the phase k , respectively ($\tilde{\cdot}$ denotes dimensional quantities). The assumption of continuous phase distributions is implicit in Eq. (1).

Similarly, the momentum conservation equation for phase k reads

$$\frac{D}{D\tilde{t}} (\alpha_k \rho_k \tilde{\mathbf{u}}_k) = -\alpha_k \nabla \tilde{p} + \nabla \cdot \alpha_k \tilde{\boldsymbol{\tau}}_k + \alpha_k \rho_k g \tilde{\mathbf{k}} + \tilde{\mathbf{M}}_k, \quad (2)$$

where \tilde{p} is pressure, taken to be equal in each phase.³⁵ $\nabla \cdot \alpha_k \tilde{\boldsymbol{\tau}}_k$ are the molecular and turbulent diffusive terms for phase k , $g = -9.8 \text{ m s}^{-2}$ is the gravity acceleration acting in the vertical direction aligned with coordinate z , and $D/D\tilde{t} = \partial/\partial\tilde{t} + \tilde{\mathbf{u}} \cdot \nabla$. $\tilde{\mathbf{M}}_k$ accounts for the momentum transfer between phases and we require

$$\sum_k \tilde{\mathbf{M}}_k = 0, \quad (3)$$

i.e., phase interactions within the fluid do not affect the bulk momentum.

We consider here that there are only two discrete phases, a liquid carrier phase (l) and a gas bubbles phase (b), so that $\tilde{\mathbf{M}}_l = -\tilde{\mathbf{M}}_b$ and $\alpha_b + \alpha_l = 1$. The gas phase density ρ_b is assumed to be constant and much smaller than that of the liquid phase. In addition, we assume that the maximum values of gas volume fraction, found at the source, are small enough to satisfy the Boussinesq approximation.^{33,36} With these assumptions the liquid phase mass conservation equation reduces to

$$\nabla \cdot \tilde{\mathbf{u}}_l = 0. \quad (4)$$

The liquid carrier phase momentum is obtained by summing the momentum equations for both phases (see Ref. 20 for details). Neglecting the gas phase contribution given the vanishing density

ratio relative to the liquid yields

$$\bar{\rho}_w \frac{D\tilde{\mathbf{u}}_l}{D\tilde{t}} = -\nabla\bar{p} + \nabla \cdot \tilde{\boldsymbol{\tau}}_l + \alpha_l \rho_l \mathbf{g}, \quad (5)$$

where $\bar{\rho}_w$ is a reference state value and the local density, assuming small values of gas volume fraction $\alpha_b = 1 - \alpha_l$, is approximated as $\rho \approx \alpha_l \rho_l = (1 - \alpha_b) \rho_l$.

The mass conservation of gas can be written as

$$\frac{\partial}{\partial \tilde{t}} \alpha_b \rho_b + \nabla \cdot (\alpha_b \rho_b \tilde{\mathbf{u}}_b) = 0, \quad (6)$$

where the gas phase velocity can be decomposed into $\tilde{\mathbf{u}}_b = \tilde{\mathbf{u}}_l + \tilde{\mathbf{u}}_s + \tilde{\mathbf{u}}_d$, where $\tilde{\mathbf{u}}_s$ is the slip velocity and $\tilde{\mathbf{u}}_d$ is the drift velocity.³⁷ In agreement with experiments,³⁸ numerical simulations,³⁴ and DwH estimations,³² the slip velocity has been assumed to have only a constant vertical component, i.e., $\tilde{\mathbf{u}}_s = (0, 0, \tilde{w}_s)$.²⁰ In this work, the bubble model was intended to be kept as simple as possible and no parametrization for additional turbulent transport has been used.^{33,36} Interactions between bubbles and the influence of the liquid phase turbulence are usually accounted for using the drift velocity. With a simple model for $\tilde{\mathbf{u}}_d$, the gas phase velocity reduces to

$$\tilde{\mathbf{u}}_b = \tilde{\mathbf{u}}_l + \tilde{\mathbf{u}}_s - \mathcal{D}_b \frac{\nabla \alpha_b}{\alpha_b}, \quad (7)$$

where \mathcal{D}_b is taken to be a constant diffusivity coefficient. The mass conservation for the gas phase in Eq. (6) then yields

$$\frac{\partial \alpha_b}{\partial \tilde{t}} + \nabla \cdot (\alpha_b \tilde{\mathbf{u}}_l) = \mathcal{D}_b \nabla^2 \alpha_b - \tilde{w}_s \frac{\partial \alpha_b}{\partial \tilde{z}}. \quad (8)$$

In order to close the system, it is necessary to define an equation of state for the local liquid density ρ_l . We model here the *oil* as a miscible, idealized dispersed phase with a reference density ρ_o only slightly lower than that of the water such that $\varsigma = (\bar{\rho}_w - \bar{\rho}_o)/\bar{\rho}_w = 0.2$. As such, defining β as the oil volume fraction, the liquid density can be written as

$$\begin{aligned} \rho_l &= \beta \rho_o + (1 - \beta) \rho_w = \\ &= \beta \bar{\rho}_o \left(1 - \gamma_o (\tilde{T} - \tilde{T}_r)\right) \\ &\quad + (1 - \beta) \bar{\rho}_w \left(1 - \gamma_w (\tilde{T} - \tilde{T}_r)\right), \end{aligned} \quad (9)$$

where the thermal expansion coefficients for water and oil are $\gamma_w = 2 \cdot 10^{-4} \text{ K}^{-1}$ and $\gamma_o = 10^{-3} \text{ K}^{-1}$ respectively and \tilde{T}_r is the reference state value.

The system is closed with two additional equations for the temperature \tilde{T} and scalar β ,

$$\frac{\partial \tilde{T}}{\partial \tilde{t}} + \nabla \cdot (\tilde{T} \tilde{\mathbf{u}}_l) = \mathcal{D}_\theta \nabla^2 \tilde{T}, \quad (10)$$

$$\frac{\partial \beta}{\partial \tilde{t}} + \nabla \cdot (\beta \tilde{\mathbf{u}}_l) = \mathcal{D}_o \nabla^2 \beta, \quad (11)$$

where \mathcal{D}_θ and \mathcal{D}_o are assumed constant.

B. Mixture model

The equation of state for the liquid phase Eq. (9) is analogous to that used in the *mixture model*³⁹ for a two liquid-liquid component system with moderate density differences. In this approach the mixture density and velocity can be written as

$$\rho_m = \beta \rho_o + (1 - \beta) \rho_w, \quad (12)$$

$$\tilde{\mathbf{u}}_m = \frac{\beta \rho_o \tilde{\mathbf{u}}_o + (1 - \beta) \rho_w \tilde{\mathbf{u}}_w}{\rho_m}, \quad (13)$$

where $\tilde{\mathbf{u}}_o$ and $\tilde{\mathbf{u}}_w$ are the oil and water liquid phase velocities.

Substituting the mixture definitions above in the conservation equations (1) and (2) and assuming the Boussinesq approximation yields³⁶

$$\nabla \cdot \tilde{\mathbf{u}}_m = 0 \quad (14)$$

and

$$\bar{\rho}_w \frac{D\tilde{\mathbf{u}}_m}{Dt} = \nabla \tilde{p} + \nabla \cdot \tilde{\boldsymbol{\tau}}_m + \rho_m \mathbf{g} + \nabla \cdot \left[\beta \rho_o \left(1 - \frac{\beta \rho_o}{\rho_m} \right) \tilde{\mathbf{u}}_r \tilde{\mathbf{u}}_r \right], \quad (15)$$

where $\tilde{\mathbf{u}}_r = \tilde{\mathbf{u}}_o - \tilde{\mathbf{u}}_w$ is the relative velocity of the oil and water phases. If the oil moves with the carrier phase, $\tilde{\mathbf{u}}_r \approx 0$, Eqs. (15) and (5) are equivalent except for the specific form of the equation of state and the interpretation of the Fickian diffusion in Eq. (11).

C. Non-dimensional equations

The background environment is thermally stratified with a constant slope ζ . The temperature can be decomposed into $\tilde{T}(\tilde{\mathbf{x}}, \tilde{t}) = \tilde{\theta}(\tilde{\mathbf{x}}, \tilde{t}) + \tilde{T}_r + \zeta \tilde{z}$, where $\tilde{\theta}(\tilde{\mathbf{x}}, \tilde{t})$ is the disturbance with respect to the unperturbed environment with temperature $\tilde{T}_e(\tilde{z}) = \tilde{T}_r + \zeta \tilde{z}$ and density $\rho_e = \bar{\rho}_w(1 - \gamma_w(\tilde{T}_e - \tilde{T}_r)) = \bar{\rho}_w(1 - \gamma_w \zeta \tilde{z})$. The corresponding buoyancy frequency N is then

$$N^2 = -\frac{g}{\bar{\rho}_w} \frac{d\rho_e}{d\tilde{z}} = g\zeta\gamma_w. \quad (16)$$

The system of transport equations (4), (5), (8), (10), and (11) are non-dimensionalized using the usual scales for stratified plumes, namely, $U_0 = (B_0 N)^{1/4}$, $t_0 = 1/N$, $L_0 = (B_0/N^3)^{1/4}$, $p_0 = \bar{\rho}_w U_0^2$, and $T_0 = \zeta L_0 \equiv (B_0 N^5)^{1/4}/(g\gamma_w)$ for velocity, time, length, pressure and temperature respectively.

The inlet buoyancy flux B_0 is defined as

$$B_0 = g_0' \tilde{Q} = g \rho_0' \tilde{Q} = g \frac{(\rho_e - \rho)|_{z=0}}{\bar{\rho}_w} \tilde{Q} \approx g \tilde{A} \tilde{w}_0 \left[\alpha_{b,0} + \varsigma \beta_0 + \gamma_w \tilde{T}_0 + \xi \beta \gamma_w (\tilde{\theta} + \zeta \tilde{z}) \right] = g \tilde{A} \tilde{w}_0 b_0, \quad (17)$$

where \tilde{Q} is the volume flux, $\tilde{A} = \pi \tilde{D}^2/4$ is the cross section area of a circular source of diameter \tilde{D} , the parameter $\xi = (\bar{\rho}_o \gamma_o - \bar{\rho}_w \gamma_w)/(\bar{\rho}_w \gamma_w)$ accounts for differences in the thermal expansion coefficient between oil and water, and \tilde{w}_0 , $\tilde{T}_0 \equiv \tilde{\theta}_0$, $\alpha_{b,0}$, β_0 , and b_0 are the inlet liquid phase velocity, temperature, gas volume fraction, oil volume fraction, and total density defect term respectively.

Note that the density perturbation, written as

$$\rho' = \frac{\rho_e - \rho}{\bar{\rho}_w} = \alpha_b + \varsigma \beta + \gamma_w \tilde{\theta} + \xi \beta \gamma_w (\tilde{\theta} + \zeta \tilde{z}), \quad (18)$$

includes the non-linear term, $\xi \beta \gamma_w (\tilde{\theta} + \zeta \tilde{z})$. A second non-linear term, $\varsigma \alpha \beta$, has been neglected due to the very small values of gas volume fraction assumed.

The final non-dimensional system of partial differential equations reads

$$\nabla \cdot \mathbf{u} = 0, \quad (19)$$

$$\frac{D\mathbf{u}}{Dt} = -\nabla p + \frac{1}{Re} \nabla^2 \mathbf{u} + [Ri(\alpha_b + \varsigma \beta) + \theta + \xi \beta(\theta + z)] \vec{k}, \quad (20)$$

$$\frac{D\theta}{Dt} = \frac{1}{Pe_T} \nabla^2 \theta - w, \quad (21)$$

$$\frac{D\alpha_b}{Dt} = \frac{1}{Pe_b} \nabla^2 \alpha_b - U_N \frac{\partial \alpha_b}{\partial z}, \quad (22)$$

$$\frac{D\beta}{Dt} = \frac{1}{Pe_o} \nabla^2 \beta, \quad (23)$$

where the non-dimensional groups are the Reynolds number $Re = U_0 L_0 / \nu = \sqrt{B_0 N} / (N \nu)$, the Péclet number for a scalar $mPe_m = U_0 L_0 / \mathcal{D}_m = \sqrt{B_0 N} / (N \mathcal{D}_m)$, the Richardson number $Ri = g L_0 / U_0^2 = g / (B_0^{1/4} N^{5/4})$, and the non-dimensional slip velocity $U_N = w_s / U_0$. Given the negligible

diffusive transport²⁰ and neglecting any double diffusion effects, we set the kinematic viscosity and diffusivity for each scalar m to be $\nu = \mathcal{D}_m = 10^{-6} \text{ m}^2 \text{ s}^{-1}$. Non-dimensional coordinates, time, velocity, pressure, and temperature are represented by $\mathbf{x} = (x, y, z)$, t , \mathbf{u} , p , and T (or θ for the perturbation) respectively. The subindex l for the liquid phase has been dropped for clarity.

The system in Eqs. (19)-(23) contains Equations (21)-(23) for the three scalars that set the three possible buoyancy sources associated with temperature (θ), gas volume fraction (α_b), and/or oil volume fraction (β). The three equations differ in their right hand side terms where the action of the slipping gas is accounted for in Eq. (22) whereas the effect of the stratification appears only in Eq. (21).

D. Integral models

In order to obtain a solvable set of equations, in the derivation of the classical integral model it is assumed, in addition to the Boussinesq approximation, that (i) the rate of entrainment into the plume is proportional to some characteristic vertical velocity at a given height and (ii) the profiles of mean vertical velocity and buoyancy force in horizontal sections are self-similar in the vertical.

The non-dimensional mean volume (Q), momentum (M), and buoyancy (B) fluxes are

$$Q(z) = 2\pi \int_0^\infty r \langle w \rangle(r, z) dr, \quad (24)$$

$$M(z) = 2\pi \int_0^\infty r \langle w \rangle^2(r, z) dr, \quad (25)$$

$$\begin{aligned} B(z) &= 2\pi \int_0^\infty r \langle w \rangle(r, z) \langle g' \rangle(r, z) dr = \\ &= 2\pi \int_0^\infty r \langle w \rangle(r, z) \langle \theta \rangle(r, z) dr + \\ &\quad + 2\pi Ri_S \int_0^\infty r \langle w \rangle(r, z) \langle \beta \rangle(r, z) dr + \\ &\quad + 2\pi Ri \int_0^\infty r \langle w \rangle(r, z) \langle \alpha_b \rangle(r, z) dr = B_T + B_o + B_b, \end{aligned} \quad (26)$$

where the buoyancy flux B has been split into three different possible buoyancy sources, namely, thermal (B_T), due to the presence of an oil phase (B_o), or a gas phase (B_b). Assuming Gaussian, self-similar profiles, the mean vertical velocity, and scalar fields can be written as

$$\langle w \rangle(r, z) = \langle \hat{w} \rangle(z) e^{-(r/b(z))^2}, \quad (27)$$

$$\langle \theta \rangle(r, z) = \langle \hat{\theta} \rangle(z) e^{-(r/\lambda_T b(z))^2}, \quad (28)$$

$$\langle \beta \rangle(r, z) = \langle \hat{\beta} \rangle(z) e^{-(r/\lambda_o b(z))^2}, \quad (29)$$

$$\langle \alpha_b \rangle(r, z) = \langle \hat{\alpha}_b \rangle(z) e^{-(r/\lambda_b b(z))^2}, \quad (30)$$

where the “hat” symbol denotes the mean centerline value and λ_T , λ_o , and λ_b are the ratios of the each scalar plume width to that of the momentum plume $b(z)$.⁴⁰⁻⁴²

Integrating the time averaged, axisymmetric, and non-dimensional forms of the transport equations (19)-(23) in the radial direction and neglecting the diffusive terms yields

$$\frac{dQ}{dz} = (8\pi)^{1/2} \alpha M^{1/2}, \quad (31)$$

$$\begin{aligned} \frac{dM}{dz} &= \frac{1}{\gamma_M} \frac{Q}{M} \left(\frac{\lambda_T^2 + 1}{2} B_T + \frac{\lambda_o^2 + 1}{2} B_o + \frac{\lambda_b^2 + 1}{2} B_b \right) \\ &\quad - 2\pi \frac{d}{dz} \int_0^\infty (\langle w'^2 \rangle - \langle u'^2 \rangle) r dr, \end{aligned} \quad (32)$$

$$\frac{dB_T}{dz} = -Q - 2\pi \frac{d}{dz} \int_0^\infty \langle w' \theta' \rangle r dr, \quad (33)$$

$$\frac{dB_o}{dz} = -2\pi Ri_S \frac{d}{dz} \int_0^\infty \langle w' \beta' \rangle r dr, \quad (34)$$

$$\frac{dB_b}{dz} = -2\pi Ri \frac{d}{dz} \int_0^\infty (U_N \langle \alpha_b \rangle + \langle w' \alpha'_b \rangle) r dr, \quad (35)$$

where the entrainment coefficient α has been used to relate the characteristic vertical velocity (\hat{w}) of a plume of width b to the entraining velocity in the radial direction ($\langle u \rangle$) using $(r\langle u \rangle)|_\infty = -\alpha b \langle \hat{w} \rangle$. In Eqs. (31)-(35) the radial turbulent flux terms are absent by construction. Using standard scaling of the mean radial momentum equation,^{5,6} the mean vertical pressure gradient has been approximated as $-\partial \langle p \rangle / \partial z \approx \partial \langle u'^2 \rangle / \partial z$. A momentum amplification factor γ_M has also been included to account for differences between the total momentum flux and the momentum flux carried by the resolved, mean flow. While in single phase plumes, this value is close to the unity, γ_M may take values up to 2.8 for bubble plumes¹⁹⁻²¹ reflecting increased turbulence in the presence of gas bubbles. Notably, the λ_i parameters modeling differences in spreading rates between momentum and scalar plumes appear only in the integral momentum flux equation, and only because it is necessary to express the buoyancy acceleration in terms of the known quantities Q , M and B . In the derivation of Eqs. (31)-(35) the radial integral of the thermal buoyancy term has been expressed in terms of the integral fluxes as

$$2\pi \int_0^\infty \langle \theta \rangle r dr = \pi \hat{\theta} \lambda_T^2 b^2 = \frac{(\lambda_T^2 + 1) B_T Q}{2 M}, \quad (36)$$

and in a similar way, the buoyancy term due to the presence of gas yields

$$2\pi Ri \int_0^\infty \langle \alpha_b \rangle r dr = \pi Ri \hat{\alpha}_b \lambda_b^2 b^2 = \frac{(\lambda_b^2 + 1) B_b Q}{2 M}. \quad (37)$$

The system in Eqs. (31)-(35) is open due to the turbulent flux terms in the vertical in Eqs. (32)-(35) and the term explicitly depending on the gas volume fraction α_b in Eq. (35). In the classical derivation, the turbulent vertical flux terms are assumed negligible and dropped. The system can then be closed by relating the gas volume fraction α_b to known quantities. This can be done by using an appropriate equation of state usually approximated via the ideal gas law and hydrostatic conditions^{18,21,30} or assuming negligible effects due to the relatively small value of the slip velocity.⁴³

Alternately, gas-slip terms in the integral solution of the governing model can be closed directly using Eq. (37) giving

$$\frac{dQ}{dz} = (8\pi)^{1/2} \alpha M^{1/2}, \quad (38)$$

$$\frac{dM}{dz} = \frac{1}{\gamma_M} \frac{Q}{M} \left(\frac{\lambda_T^2 + 1}{2} B_T + \frac{\lambda_o^2 + 1}{2} B_o + \frac{\lambda_b^2 + 1}{2} B_b \right), \quad (39)$$

$$\frac{dB_T}{dz} = -Q, \quad (40)$$

$$\frac{dB_o}{dz} = 0, \quad (41)$$

$$\begin{aligned} \frac{dB_b}{dz} &= -2\pi Ri \frac{d}{dz} \int_0^\infty U_N \langle \alpha_b \rangle r dr = \\ &= -U_N \frac{\lambda_b^2 + 1}{2} \frac{d}{dz} \left(\frac{B_b Q}{M} \right) = \\ &= -\frac{U_N (\lambda_b^2 + 1) B_b}{2M^2 + U_N (\lambda_b^2 + 1) Q M} \left(M \frac{dQ}{dz} - Q \frac{dM}{dz} \right). \end{aligned} \quad (42)$$

Defining B_λ as the λ -weighted buoyancy flux (term in parentheses in Eq. (39)), Eq. (42) can be written as

$$\frac{dB_b}{dz} = (8\pi)^{1/2} \alpha \frac{U_N(\lambda_b^2 + 1)B_b M^{1/2}}{2 + U_N(\lambda_b^2 + 1)Q} \left(\frac{1}{\gamma_M(8\pi)^{1/2} \alpha} \frac{B_\lambda Q^2}{M^{5/2}} - 1 \right). \quad (43)$$

Notably, the non-dimensional group $B_\lambda Q^2 M^{-5/2}$ has been used to characterize the nature of a plume based on the relative importance of the volume, momentum, and buoyancy fluxes at the source. Defining the source parameter Γ as

$$\Gamma = \frac{1}{(8\pi)^{1/2} \alpha \gamma_M} \frac{B_\lambda Q^2}{M^{5/2}}, \quad (44)$$

the plumes can be classified as *lazy* ($\Gamma > 1$) when there is a deficit in the momentum when compared to the pure plumes ($\Gamma = 1$) or *forced* ($\Gamma < 1$) otherwise.^{44,45} Using Eq. (44), the equation for the vertical evolution of the buoyancy flux due to the presence of gas can be rewritten as

$$\frac{dB_b}{dz} = (8\pi)^{1/2} \alpha \frac{U_N(\lambda_b^2 + 1)B_b M^{1/2}}{2 + U_N(\lambda_b^2 + 1)Q} (\Gamma - 1). \quad (45)$$

In the absence of gas (setting $\gamma_M \approx 1$), the previous system of equations can be simplified further yielding

$$\frac{dQ}{dz} = (8\pi)^{1/2} \alpha M^{1/2}, \quad (46)$$

$$\frac{dM}{dz} = \frac{Q}{M} (B_T + B_o) = \frac{BQ}{M}, \quad (47)$$

$$\frac{dB_T}{dz} = -Q, \quad (48)$$

$$\frac{dB_o}{dz} = 0 \quad (49)$$

where the total buoyancy flux is simply the sum of the individual contributions, $B = B_T + B_o$, and $d(B_T + B_o)/dz = dB/dz = -Q$. This solution is identical to that derived by Morton *et al.*⁸ for a thermal plume in both uniform and linearly stratified backgrounds.

III. NUMERICS

A. Setup

The model presented in Sec. II is used to study the differences between plumes generated by varying the distinct contributions to the inlet buoyancy flux B_0 . This is achieved by considering three different cases summarized in Table I. The only difference between these plumes is the relative contribution to B_0 from each source: oil ($f_o = \zeta \beta_0/b_0$) or gas ($f_b = \alpha_0/b_0$). The parameters $B_0 = 5 \cdot 10^{-6} \text{ m}^4 \text{ s}^{-3}$, $N = 0.1 \text{ s}^{-1}$, $U_N = 0.6$, $Ri \approx 3700$, $Re = Pe_m \approx 7100$, $D = 0.3$, and $w_0 = 1.5$ are kept the same in all experiments. The parameter space defined by these values is close to typical experimental conditions.²³ In dimensional units, this configuration corresponds to a tank of 2.6 m height with a source of 8 cm in diameter and a total temperature gradient due to stratification of 13.3 K. Defining the inlet momentum flux as $M_0 = (\pi/4)D^2 w_0^2$, the Morton length scale is $L_M = M_0^{3/4} B_0^{-1/2} \approx 0.07 \text{ m}/L_0 = 0.25^6$ suggesting that the transition from jet to buoyant plume occurs relatively close to the source.

The set of cases in Table I include plumes in which B_0 is entirely due to the presence of oil (case O) or gas bubbles (case B), and a *hybrid* plume (case H) in which B_0 is set by a combination of both forcings.

Cases B and H correspond to bubble plumes where the non-dimensional slip velocity has been set to $U_N = 0.6$. This choice is close to the value used in Ref. 20 for air bubbles with nominal

TABLE I. Inlet buoyancy flux contributions (thermal, gas, and oil phases) for the three cases studied.

Case	f_o	f_g	U_N
O	1	0	...
B	0	1	0.6
H	1/2	1/2	0.6

diameter $d_p = 2.5$ mm. Similar values have been used in investigations of rise times and entrainment heights in deepwater blowouts.³² According to the standard classification scheme,^{17,23} this non-dimensional slip velocity should produce a Type 1* plume where the liquid phase *peeling* flow is strong enough to distort the rising bubbles, resulting in an appreciable widening of an inner gas phase plume and the presence of a distinct primary intrusion level.

B. Domain and boundary conditions

The computational domain consists of a cylinder of diameter $D = 2R = \tilde{D}/L_0 = 10$ and height $H = \tilde{H}/L_0 = 10$ (aspect ratio 1). The domain is decomposed into $K = 7540$ spectral elements arranged in 20 vertical slabs of 377 elements (see a slice of the conforming element mesh in Fig. 1). Within each element, the solution is approximated with an $N = 14$ th order Legendre expansion resulting in a total of $K \times (N + 1)^3 \approx 25 \times 10^6$ degrees of freedom.

Contrary to experiments, necessarily conducted in finite size tanks, numerical solutions allow a semi-infinite domain in the horizontal which (i) avoids the filling problem due to the accumulation of scalars in the tank, (ii) permits the establishment of fully developed flow conditions and converged time averages in the numerical domain, and (iii) more closely mimics the conditions of an environmental release. Numerically this is achieved via outflow boundary conditions on the lateral walls for the momentum equation and Dirichlet zero for the scalars (θ , α_b , and β) mimicking far field conditions. In order to ensure numerical stability, the open boundaries are combined with *sponge* regions⁴⁶ in the radial direction where the local Reynolds and Péclet numbers are decreased to damp momentum and scalar perturbations arriving at the lateral boundaries. The top boundary is no-shear for the momentum and zero derivative for the scalars while constant Dirichlet boundary conditions are imposed on the bottom at the plume source. Tests conducted for rotating plumes at large Rossby numbers ($Ro = 40$) show that solutions are independent of the radial extent when R varies from 5 to 8.⁴⁷

To facilitate the transition to turbulence in the vicinity of the source, a 5% amplitude noise was added to the vertical velocity.^{9,48,49} This small forcing was applied over a cylindrical volume with a radius equal to that of the source and a height equivalent to $H/40$.

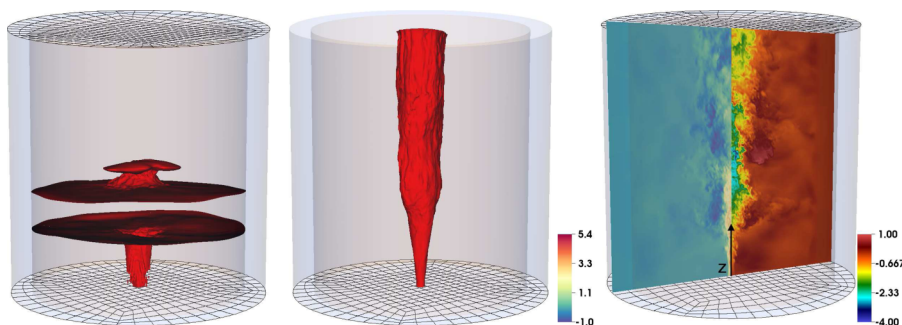


FIG. 1. Left panel: isosurfaces of time averaged β ($\Delta t \approx 25$) for case O. Central panel: isosurface of time averaged α_b for case B. Right panel: slice of instantaneous w and θ (left and right halves of the right panel) for case B. Black lines show the spectral element grid. Note that there are $N = 14^2$ polynomial nodes in each element.

The first panel of Fig. 1 shows the extent of the complete domain as a semitransparent volume. The inner cylinder corresponds to the region of interest with the outer ring corresponding to the extent of the numerical sponge. An isosurface of β for case O is used to visualize the trapping height topology. The second panel shows an isosurface of the gas volume fraction α_b for case B extending across the water column. Both isosurfaces correspond to mean fields obtained by time averaging over $\Delta t \approx 25$ time units. The third panel shows an instantaneous snapshot of w (left half) and θ (right half) for the bubble plume (case B). A slice of the spectral element grid used in all computations is given at the bottom of each figure.

C. Numerical solver

The transport equations (19)-(23) are solved using the Spectral Element Method (SEM) code Nek5000.⁵⁰ This code has been validated for a wide range of flow configurations and has demonstrated excellent scalability on parallel machines, thus allowing explicit resolution of a broad range of spatial and temporal scales. SEM overcomes the geometric and boundary condition restrictions imposed by standard fully spectral methods and allows for high-order solutions on complex grids.⁵¹ Instead of explicitly modelling subgrid scales (SGS) via available Smagorinsky eddy diffusivity models,^{52,53} we use the spectral vanishing viscosity technique⁵⁴ and progressively filter the near-grid scale coefficients in the spectral polynomial expansion.^{51,55} This is equivalent to selectively reducing the nominal Reynolds and Péclet numbers at near-grid scales. A 5% polynomial filtering of the two highest modes in the 14th order Legendre expansion has been used for all the fields. The procedure ensures numerical stability and preserves the exponential convergence of the solver while avoiding the computational cost associated with computing the SGS terms. Examples of this procedure for fully developed channel configurations has shown excellent agreement with Direct Numerical Simulations (DNS), relative insensitivity to the specific form of the filter, and overall computational efficiency.⁵⁶

Fig. 2 shows the power spectrum for the vertical velocity w at $(r, z) = (0, 4)$ for case B. The peak corresponds to the *effective* nondimensional buoyancy frequency slightly larger than that of the nominal value ~ 1 due to the destratification generated by the turbulent plume. The inertial range, characterized by a $-5/3$ slope decay, is seen to span approximately one decade in frequency.

D. Averaging

The volume integral of the temperature perturbation θ and oil volume fraction β (with a negative sign for clarity) are shown in Fig. 3(a) as solid (left y axis) and dashed lines (right y axis), respectively. The results for θ indicate that as the amount of bubbles increases, the

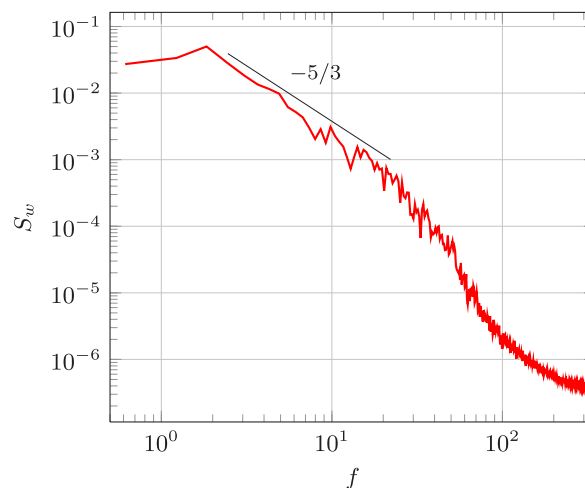


FIG. 2. Vertical velocity power spectrum at $(r, z) = (0, 4)$ for case B.

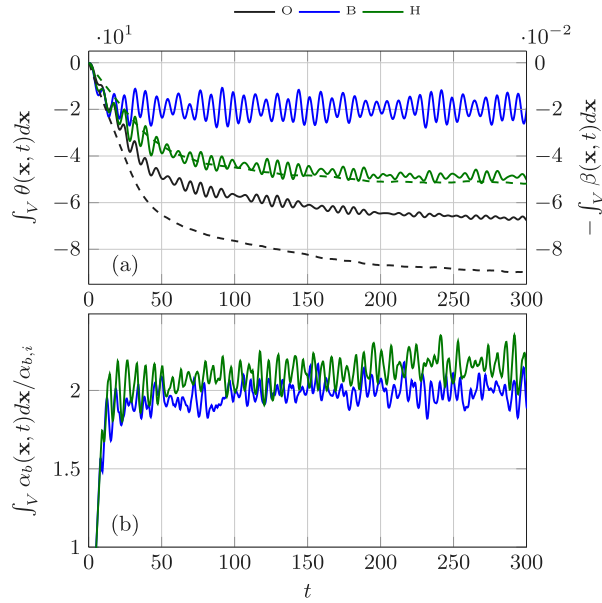


FIG. 3. Top panel: temporal evolution of the volume integral of the temperature fluctuation θ (solid) and oil volume fraction β (dashed). Bottom panel: temporal evolution of the volume integral of gas volume fraction α_b .

time required to achieve statistically steady conditions is reduced. This difference is due to the shorter transient imposed by the slipping bubbles that span the first 16 time units corresponding to the average time required by the bubbles to leave the domain through the top boundary as shown in Fig. 3(b). The required integration time to achieve dynamically steady conditions is much longer when the oil is added (see dashed lines in Fig. 3(a)). Unlike the bubbles, this scalar does not slip but instead accumulates in the domain during the formation of the lateral intrusion. The lighter oil is trapped once the temperature of the liquid phase is low enough to reach a neutral buoyancy level. Consequently the oil plumes exhibit a *cold* intrusion with the lowest terminal values of the volume integral of θ (Fig. 3(a)) corresponding to the largest inlet oil volume fraction.

The time scale imposed by the stratification is clearly observed in the perturbation temperature signal in Fig. 3(a). The continuous overshoot/downdraft generates gravity waves with frequencies close to that of the (non-dimensional) buoyancy frequency $f \approx 1$.

The pure bubble plume is characterized by the largest overshoots generated by the escaping secondary phase leading to the largest amplitudes in the volume integral of θ . This time scale is not observed in Fig. 3(b) due to the slipping nature of the bubbles. Given that Eq. (22) is homogeneous in α_b , the curves for the gas volume fraction in Fig. 3(b) collapse when scaled by their corresponding inlet values.

The integral metrics in Fig. 3 were used to determine the establishment of statistically stationary regimes. Once these conditions were reached ($t \approx 150$ for case O and $t \approx 250$ for the rest), Eulerian temporal averages interpolated on a $(n_r \times n_z) = (200 \times 100)$ uniform grid in the radial and vertical direction spanning over $r = [0, 2.5]$ and $z = [0, 10]$ were collected over times spans $\Delta t \approx 100$. Additionally, we take advantage of the axisymmetric nature of the plume to increase the sampling by averaging in the azimuthal coordinate $\phi = \tan^{-1}(y/x)$. Using cylindrical coordinates where the radial velocity is defined as $u_r(r, \phi, z) = \cos(\phi)u(x, y, z) + \sin(\phi)v(x, y, z)$, the average of any quantity ψ is given by

$$\langle \psi \rangle(r, z) = \frac{1}{\Delta t} \int_0^{2\pi} \int_0^{\Delta t} \psi(r, \phi, z, \tau) d\tau d\phi. \quad (50)$$

IV. RESULTS

A. Validation: Bubble plumes

The model presented in Section II is validated by comparing the numerical results with the isothermal bubble plume experiments reported in Ref. 23 where, by considering bubbles with different slip velocities, plumes were classified according to the topological types originally described by Asaeda and Imberger.¹⁷ Type 1* plumes, with relatively small values of U_N , produce a clearly differentiated lateral intrusion layer at the first peeling height. When the gas bubbles move slowly enough with respect to the liquid phase, the peeling downdrafts significantly perturb the gas volume fraction field resulting in the widest bubble plumes. As the slip velocity increases, plumes transition to Type 2 characterized by significantly narrower gas-phase plumes at all heights. Concentration of the bubble-plume allows the generation of distinct, secondary intrusions. Type 3 plumes are generated by even larger slip velocities where, instead of isolated trapping heights, the plume exhibits a collection of overlapping intrusions and a very narrow bubble plume.

Following the approach used in experiments, liquid-phase intrusion levels are visualized by injecting a non-slipping passive tracer along with the gas phase at the source. Figure 4 shows direct comparisons of the numerical model with experimental images for values of non-dimensional slip velocity $U_N = (1.5, 2.2, 4.7)$ corresponding to Type 1*, 2, and 3 plumes. The experimental results (right column) show instantaneous contours of the passive scalar and the bubble fields simultaneously. For clarity, volume renderings of the two fields are shown separately for the numerical results: passive dye field in blue (left column) and gas volume fraction in black (central column).

The evolution with increasing slip velocity of the overall model plume topology is in very good agreement with the experimental results. As reported in Ref. 20 quantitative numerical predictions of entrainment coefficients, momentum amplification factors and bubble/momentum plume width ratios are also in agreement with experiments. Although analogous to the cases in Table I, the plumes in Ref. 20 were generated by values of B_0 , four orders of magnitude larger than the current ones, resulting in plumes barely affected by the stratification across the computational domain.

B. Characteristic vertical plume scales

In stratified environments, plume shape and extent can be characterized using several vertical length scales shown schematically for single phase and bubble plumes in Fig. 5. As a turbulent plume evolves in the vertical, it entrains ambient fluid. Turbulent mixing erases the density defect reducing the buoyancy flux. The equilibrium height z_{eq} is defined as the distance from the source where the centerline (axial) reduced gravity (or density perturbation with respect the background) vanishes, i.e., $\langle \hat{g}' \rangle(z = z_{eq}) = 0$.⁸

Due to inertia, the plume core continues to rise above the equilibrium height, and the positively buoyant plume transitions into a negatively buoyant fountain. In a gas-free case, the plume is eventually brought to rest at the maximum vertical rise level, z_{max} , defined as the distance where the centerline mean vertical velocity vanishes $\langle \hat{w} \rangle(z = z_{max}) = 0$.⁸ While the mean volume flux is zero at

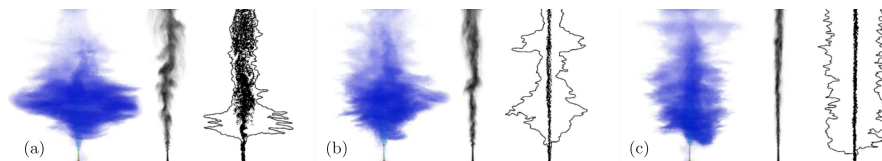


FIG. 4. Comparison of current numerical simulations for a pure bubble plume (case B) and experiments²³ for different slip velocities $U_N = 1.5, 2.2, 4.7$ from left to right, respectively. The numerical results are shown as volume renderings of the passive dye (left subpanel, in blue) and the bubble plumes (central subpanel, in black). The experimental results in the work of Socolofsky and Adams²³ are shown in the third subpanel as sketches where the isolines correspond to the dye plume and the black dots correspond to bubbles. Reprinted with permission from S. A. Socolofsky and E. E. Adams, "Role of slip velocity in the behavior of stratified multiphase plumes," *J. Hydraulic Eng.* **131**, 273-282 (2005). Copyright 2005 American Society of Civil Engineers.

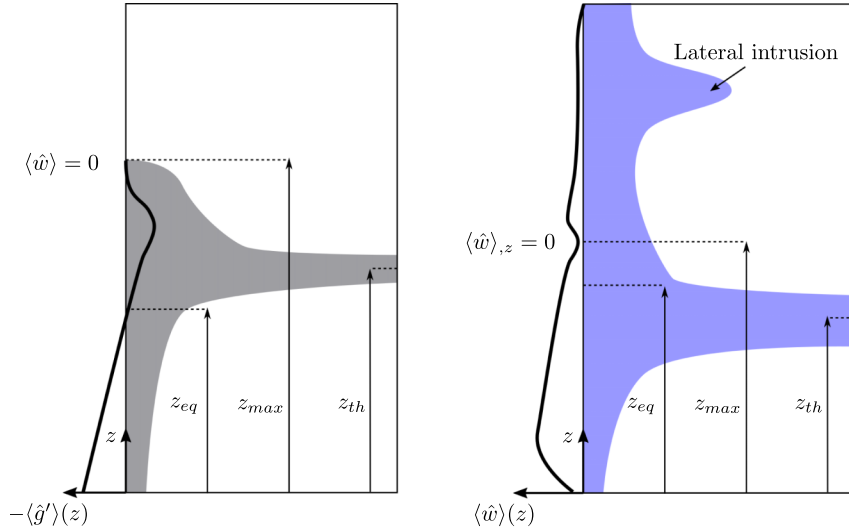


FIG. 5. Sketch of a single phase plume (left) and a bubble plume (right) in a stratified environment showing the different characteristic heights: z_{eq} where the axial mean density anomaly vanishes, z_{th} where the concentration of dyed trapped fluid in the lateral intrusion reaches a maximum, and z_{max} where the axial mean vertical velocity vanishes (single phase, left) or it reaches the first minimum (bubble plume, right).

some height in the absence of gas, bubble plumes (cases B and H) continue to destratify the background flow generating additional entrainment/detrainment regions associated with the formation of secondary intrusions (see Fig. 4). Although the mean centerline velocity does not vanish at any height, it does reach a local minimum. We define z_{max} to be the location of the first minimum of $\langle \hat{w} \rangle$ in bubble and hybrid plumes. This location corresponds to the peeling height h_P defined as the location where core plume fluid first detains, or peels, and starts to descend.²⁶

In a stably stratified environment, the plume is also characterized by the height where neutrally buoyant fluid accumulates and is transported in the horizontal. For definitiveness, we define this lateral intrusion level or trapping height, z_{th} , as the vertical location where the trapped scalar in the lateral intrusion exhibits its far field peak value, i.e., $\langle \beta \rangle(r = 2.5, z = z_{th}) = \max(\langle \beta \rangle(r = 2.5, z))$. At $r = 2.5 \approx 17R$, the radial gradients are negligible and profiles at this radial location are assumed to represent far field conditions. Evaluated on the axis and in the far horizontal field, respectively, z_{eq} and z_{th} exhibit significant differences.⁹

Using the *mixture model*, the equation of state Eq. (18) for a liquid phase with two components with negligible relative velocity and temperature-dependent densities has a non-linear term. The effects of this non-linearity are analyzed here by comparing the pure oil case with an identical plume only distinguished by a linear version of this equation of state, i.e.,

$$\rho' = \varsigma \beta + \gamma_w \tilde{\theta}. \quad (51)$$

Radial profiles of $\langle \beta \rangle$ and $\langle w \rangle$ at several vertical locations using the equation of state Eq. (18) (solid) and Eq. (51) (dashed) are shown in Fig. 6. The results indicate that the non-linear contribution is marginal and has negligible effects on mean fields. This implies that the plume driven by a non-slipping oil phase is analogous to a single phase buoyant plume in a stratified environment. In other words, instead of the volume fraction of a discrete, non-slipping liquid phase, one may consider β , an additional active scalar in a linear equation of state for a single liquid component, for example, salinity in a salinity-temperature system with ς representing the corresponding thermal expansion coefficient.

The negligible effects of the non-linear term allows for direct comparison of case O and other studies on single-phase buoyant plume in stratified environments. Experiments typically consist in injecting fresh water into a salinity stratified background^{8,57} but thermally driven plumes have also been studied experimentally⁵⁸ and numerically.⁹ Table II compares the current results with other buoyant plume studies revealing good agreement in terms of the characteristic plume rise

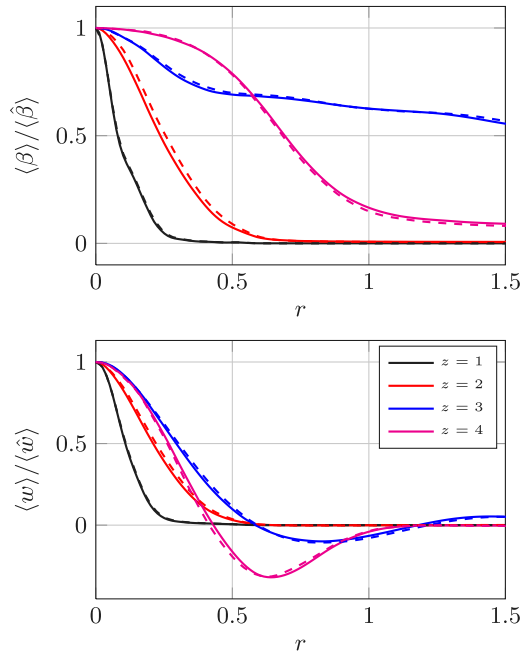


FIG. 6. Mean scalar $\langle \beta \rangle$ and vertical velocity w profiles for case O at several vertical locations using the original liquid phase equation of state (18) (solid) and the linearized version (51) (dashed). Results are normalized using the centerline value.

location z_{max} , especially in comparison to the numerical study by Devenish *et al.*⁹ Morton *et al.*⁸ and Richards *et al.*⁵⁷ do not distinguish between z_{eq} and z_{th} and use the lateral intrusion height to determine the neutral buoyancy level. As such, the corresponding results are placed under the z_{eq} column in Table II. While the results for z_{eq} show good agreement with both the experiments by Richards *et al.*⁵⁷ and the numerical simulation by Devenish *et al.*,⁹ the experiments by Morton *et al.*⁸ seem to overpredict the lateral intrusion height. Similarly, results for the ratio z_{eq}/z_{max} in excellent agreement with the work of Richards *et al.* and Devenish *et al.*, differ significantly from those reported by Morton *et al.* These discrepancies may be due to the modest radial extent of the experimental tank that necessarily limits the duration of the experiment as the dye accumulates and also may lead to the establishment of boundary-generated recirculations.

In what follows, we will be particularly interested in changes in the dynamics within the inertial overshoot region. The ratio of conditioned upward and downward volume fluxes computed in the z_{max} horizontal plane can be used to characterize the entrainment at the plume top. This ratio, $Q_{up}/Q_{down} = 0.27$, computed for the single phase plume, compares very well with the value 0.25 reported in the work of Devenish *et al.*⁹ Agreement has also been found for the location of the maximum radial extent of the negatively buoyant fountain at $z/z_{eq} \approx 1.2$.

TABLE II. Comparison of plume characteristic heights between the current work and work of Morton *et al.*⁸ ($\alpha = 0.090$), Crawford and Leonard⁵⁸ ($\alpha = 0.093$), Devenish *et al.* (interpolated from Fig. 12 in Devenish *et al.*⁹), Richards *et al.*,⁵⁷ and Tsinober *et al.*⁵⁹

Source	z_{max}	z_{eq}	z_{th}	z_{eq}/z_{max}
Current work	4.5	2.85	3.11	0.63
Morton <i>et al.</i>	4.3	3.25	...	0.76
Devenish <i>et al.</i>	4.5	2.95	...	0.66
Richards <i>et al.</i>	4.1	2.68	...	0.65
Crawford and Leonard	4.2
Tsinober <i>et al.</i>	4.4

TABLE III. Values of the characteristic heights z_{th} , z_{eq} and z_{max} , deviations with respect to the pure oil case O, and inertial overshoot height ($z_{max} - z_{eq}$) and downdraft height ($z_{max} - z_{th}$). In parenthesis the average values of trapping height $h_T \equiv z_{th}$ and the peeling height h_P from all the experiments at $U_N < 0.8$ from the work of Socolofsky and Adams.²³

Case	f_o	f_g	z_{th}	z_{eq}	z_{max}	Δz_{th}	Δz_{eq}	Δz_{max}	$z_{max} - z_{eq}$	$z_{max} - z_{th}$
O	1	0	3.1	2.8	4.50	1.65	1.39
H	1/2	1/2	2.6	3.2	4.65	-0.46	0.31	0.15	1.49	2.00
B	0	1	2.4 (2.5)	3.5	4.95 (4.5)	-0.74	0.64	0.45	1.46	2.58

The presence of gas bubbles alters the plume topology and modifies the values of the characteristic heights.²² The conservation equation for ρ' , obtained by adding the buoyancy-normalized scalar equations in Eqs. (21)-(23) (diffusive terms omitted),

$$\frac{D\rho'}{Dt} = -\frac{w}{Ri} - U_N \frac{\partial \alpha_b}{\partial z}, \quad (52)$$

indicates that, for similar values of vertical velocity, the negative vertical gradient of gas volume fraction reduces the vertical decay rate of ρ' along the axis. In effect, and as shown in Table III, the axial characteristic heights z_{eq} and z_{max} increase as the amount of bubbles grows. In comparison to the single phase case, the vertical extent of the pure bubble plume increases by 10%. Increasing the buoyancy flux carried by the gas phase, however, reduces the height of the main lateral intrusion measured by z_{th} . While both the pure bubble and hybrid plumes are taller than the gas-free case for on-axis measures, the increase in height of the inertial overshoot region leads to a decrease in the location of the lateral intrusion. The presence of gas increases the potential energy of the peeling fluid which, in turn, reinforces the downdraft recirculation in the outer plume region.

The characteristic heights in Table III and the mean fields of temperature $\langle T \rangle$ (top panels) and $\langle \beta \rangle / \beta_0$ (bottom) are shown in Fig. 7 for the three cases. The thick horizontal black lines indicate the locations of z_{th} (solid), z_{eq} (dashed) and z_{max} (dotted). The thin black lines correspond to the z_{eq} and z_{max} results by Morton *et al.*⁸ and the white dashed line indicates the average z_{th} value for $U_N = 0.6$ as reported by Socolofsky and Adams.²³

The mean temperature fields show the increase in the vertical extent of the signature as the amount of gas in the system grows. The dependence of the penetration height on the amount of bubbles is very similar to that observed in z_{max} . In comparison to the single phase case, this characteristic height values grow by 3% and 10% for cases H and B respectively (see Table III). In the oil case, $\langle T \rangle$ is locally “cold” in the lateral intrusion where the accumulation of positively buoyant β must be offset by a negative thermal signature to maintain a neutral buoyancy level. In the hybrid case in Fig. 7(H-1), with half the amount of β at the inlet, the intensity of this cold intrusion weakens. In the pure bubble case in Fig. 7(B-1) where β represents a passive scalar, the vertical profiles of $\langle T \rangle$ at any r location grow monotonically.

Mean $\langle \beta \rangle / \beta_0$ fields, shown in the bottom panels of Fig. 7, indicate the shape and extent of the lateral intrusion levels. In comparison the single phase plume, z_{th} decreases by 16% and 22% in cases H and B respectively. The intrusion levels in the bubble cases are also considerably thicker suggesting changes in the turbulent mixing in the presence of gas extend well beyond the bubble core region. Secondary intrusions above z_{max} intensify and their vertical location ($1.06z_{max}$ and $1.08z_{max}$ in cases H and B respectively) increases with the amount of gas.

These secondary intrusions in the hybrid and bubble plumes are the result of first order effects due to the gas-phase slip velocity. The gas-free case, with no explicit slip, also produces a weak secondary intrusion in the active scalar field shown in Fig. 7(O-2) As explained below, this weaker secondary intrusion of the scalar fields is due to differences in the vertical turbulent flux of the temperature and β fields in the presence of ambient thermal stratification.

The effects of the presence of a gas phase on the mean three-dimensional plume structure are shown in Fig. 8. The two isosurfaces in the top panels correspond to mean vertical velocities $\langle w \rangle = -0.15$ (blue) and $\langle w \rangle = 0.1$ (red) for cases O (left), H (center) and B (right) respectively

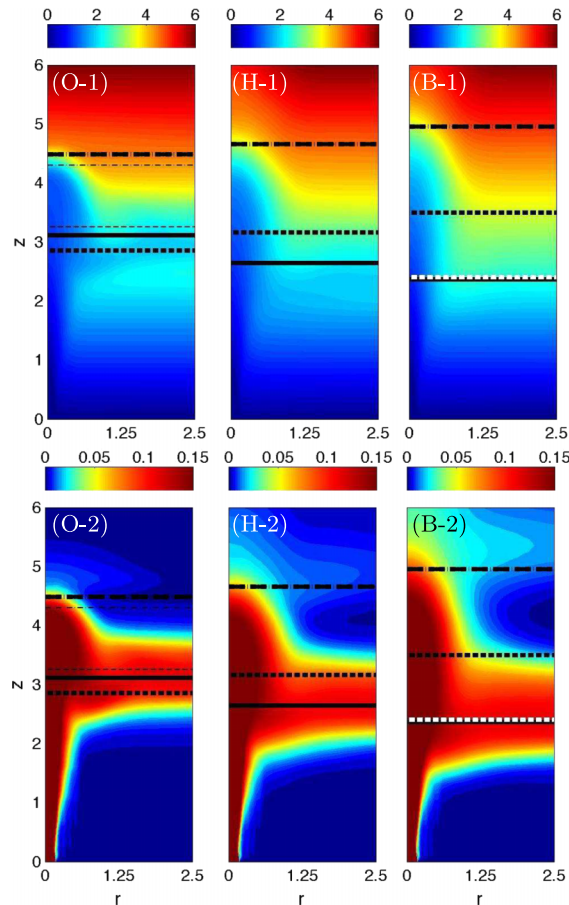


FIG. 7. Top: mean temperature $\langle T \rangle$ for a pure oil (left), hybrid (center), and pure bubble (right) plume. Bottom: normalized mean scalar $\langle \beta \rangle / \beta_0$. The characteristic heights z_{th} , z_{eq} , and z_{max} are represented by horizontal thick solid, dashed, and dotted lines respectively. Black thin lines correspond to z_{eq} and z_{max} as reported by Morton *et al.*⁸ and the white dashed line corresponds to the average value for the $U_N = 0.6$ cases in the work of Socolofsky and Adams.²³

obtained by averaging over a time period $\Delta t \approx 25$. The two isosurfaces in the bottom panels correspond to mean radial velocities $\langle u_r \rangle = -0.07$ (blue) and $\langle u_r \rangle = 0.1$ (red) for the three plumes. Fig. 8(o-1) shows the inner core of the single phase plume (in red), the outer ring of downdrafts (in blue) and a weak second ring of updrafts associated to the presence of gravity waves (in red). The vertical location of this feature at $z/z_{eq} = 1.08$ agrees well with the value found by Devenish *et al.*⁹ at $z/z_{eq} = 1.11$.

In the single-phase plume where the total buoyancy readily mixes with the environment, ambient stratification strongly constrains the vertical height of the plume. The addition of a slipping gas-phase buoyancy source produces regions of appreciable vertical velocity across the entire water column. The most prominent effect of the increased potential energy due to gas is the change in the intensity and size of the downdraft, negative vertical velocity, regions at the primary plume top (upper panels of Fig. 8). As shown in the lower panels of the figure, the larger downdrafts generate significantly stronger entrainment above z_{eq} and smaller mean axial velocities at the intrusion level. The net result, for both the hybrid and pure bubble plumes, is a lower and thicker intrusion layer.

The increased size and extent of the primary downdrafts produced by plumes with slipping buoyancy contributions are quantified by vertical profiles of $\langle w \rangle$ at two radial locations (Fig. 9). At $r = 0.6$ (solid), where the downdrafts are the most intense, the regions where $\langle w \rangle < 0$ are considerably larger for bubble and hybrid plumes although the maximum value of downwards velocity is smaller than in the single phase case. Unlike the single phase case which shows a small signature of

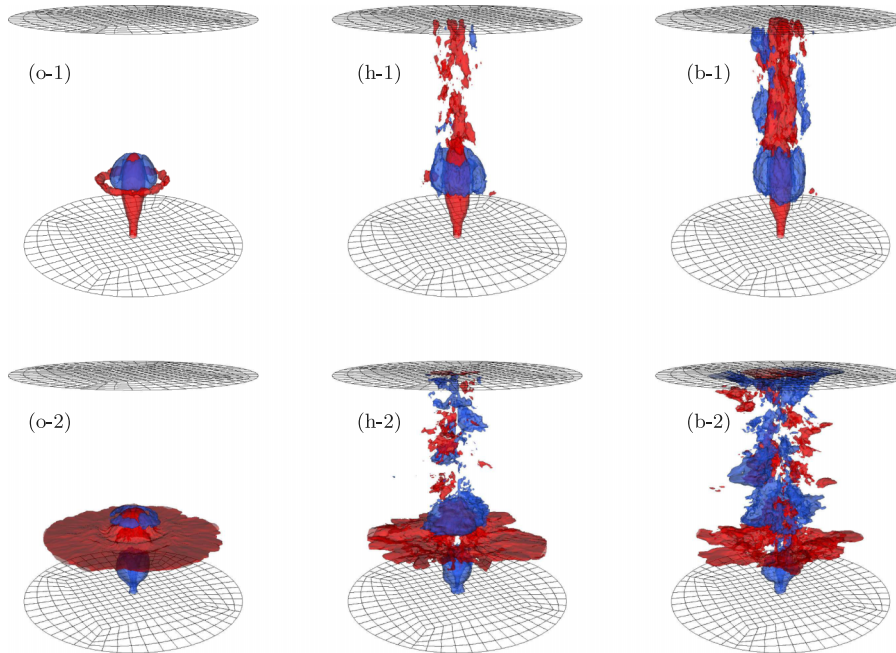


FIG. 8. Top: two mean vertical velocity isosurfaces $\langle w \rangle = 0.1$ (red) and -0.15 (blue) for cases O (left), H (center), and B (right). Bottom: two mean radial velocity isosurfaces $\langle u_r \rangle = 0.1$ (red) and -0.07 (blue).

positive vertical velocity in the beginning of the intrusion layer, the region of appreciable downdraft velocity extends beyond $r = 1.25$ in both bubble plumes (dashed lines).

The intensified downdraft and entrainment velocities observed in hybrid and bubble plumes significantly modify the turbulence in the inertial overshoot region between z_{eq} and z_{max} . Vertical profiles of turbulent kinetic energy,

$$\text{TKE} = \langle k \rangle = \frac{1}{2} \langle u'_i u'_i \rangle,$$

evaluated at the plume centerline are plotted in Fig. 10(a). Below the equilibrium level, both the hybrid and bubble plumes show modest increases in $\langle k \rangle$ over the single-phase case. As shown in Ref. 20 for very weak stratification, the gas slip-velocity results in larger turbulent shear production and increased turbulence. Differences between the single and multi-phase cases are more pronounced in the plume top where TKE is nearly two times larger in both the bubble and hybrid plumes compared to the single-phase case. Increased turbulent mixing in this region is responsible

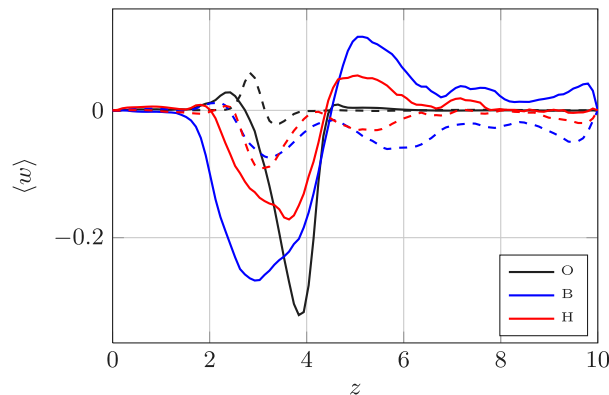


FIG. 9. Vertical velocity at $r = 0.6$ (solid) and $r = 1.25$ (dashed).

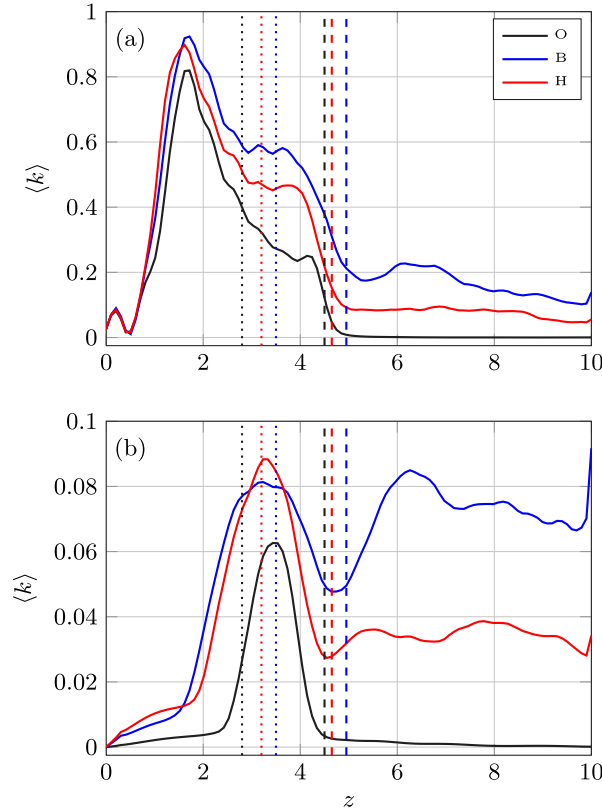


FIG. 10. Vertical evolution of the turbulent kinetic energy at $r=0$ (a) and $r=1$ (b). Characteristic heights z_{eq} and z_{max} shown as dotted and dashed vertical lines, respectively.

for the reduction in the extent of the inertial overshoot, $z_{max} - z_{eq}$, observed for cases O and H. Similar increases in turbulence levels also occur in the formation of the lateral intrusion layers as shown by the vertical profiles of TKE evaluated at $r = 1$ in Fig. 10(b).

Turbulent transport at the very top of the plume is also responsible for the secondary intrusion observed in the $\langle \beta \rangle$ and $-\langle \theta \rangle$ fields for the gas-free plume with both thermal and “oil” buoyancy contributions. As shown in Fig. 11(a), near z_{max} , mean vertical gradients of the two active scalars have opposite signs; $\partial \langle \beta \rangle / \partial z < 0$ and $\partial \langle \theta \rangle / \partial z > 0$. Since the mean flow vanishes in this region, turbulent fluxes dominate the local transport. Standard mixing length estimates, with

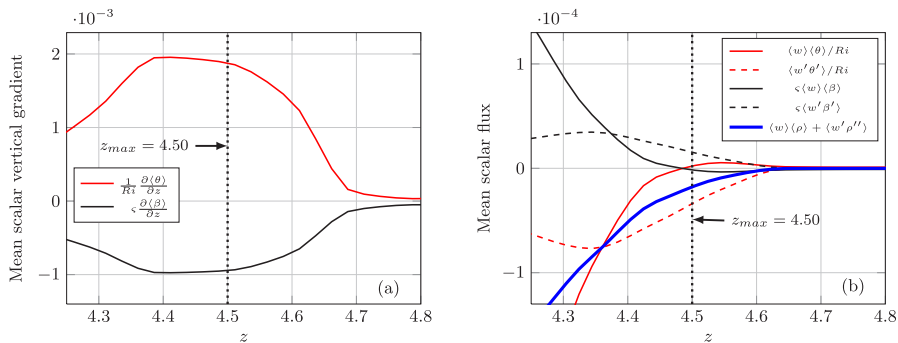


FIG. 11. (a) Centerline mean vertical gradients of θ (red) and β (black) in case O at the plume top region. (b) Centerline mean (solid) and turbulent (dashed) fluxes of θ (red) and β (black). The total vertical transport of buoyancy shown as a thick blue line. The vertical dotted line indicates the location of z_{max} .

eddy-diffusivity κ_T , imply $\langle \theta'w' \rangle \approx -\kappa_T \partial \langle \theta \rangle / \partial z < 0$ and $\langle \beta'w' \rangle \approx -\kappa_T \partial \langle \beta \rangle / \partial z > 0$. Physically, at the plume top, positive vertical velocity fluctuations are correlated with positive fluctuations of β and negative fluctuations of θ . The mean (black solid) and turbulent (black dashed) vertical fluxes of β are shown in Fig. 11(b). The net positive vertical flux of β , accompanied by a (negative) flux of θ , leads to a turbulence-driven secondary intrusion of cold “oil” above z_{max} .

C. Comparison with integral model

Given the computational expense of the turbulence resolving simulations, we would like to assess how well standard integral model formulations, explicitly derived from the simulated equation set in Sec. II D, compare to fluxes computed from the full model solutions. The vertical evolution of the area averaged volume Q , momentum M , and buoyancy B fluxes for the three plumes are shown in Fig. 12. Notably, below the equilibrium height where the self-similarity assumptions of standard integral models are expected to hold, profiles of both Q and M are very similar in the three cases. Although the bubble and hybrid plumes are taller on the axis, the increased peeling in the presence of gas bubbles significantly lowers the location and value of the maximum volume flux for cases O and H compared to the single-phase case. As shown in Fig. 12(c), larger differences between the three cases occur in the evolution of the buoyancy fluxes. As expected, the gas-phase slip velocity produces an initial increase in the buoyancy flux in the bubble cases. This increase is largest in the pure bubble case where all the initial buoyancy is concentrated in the gas. However, in the self-similar region, the vertical decay rate of buoyancy, $\frac{dB}{dz}$, is similar for all cases despite the initial offset.

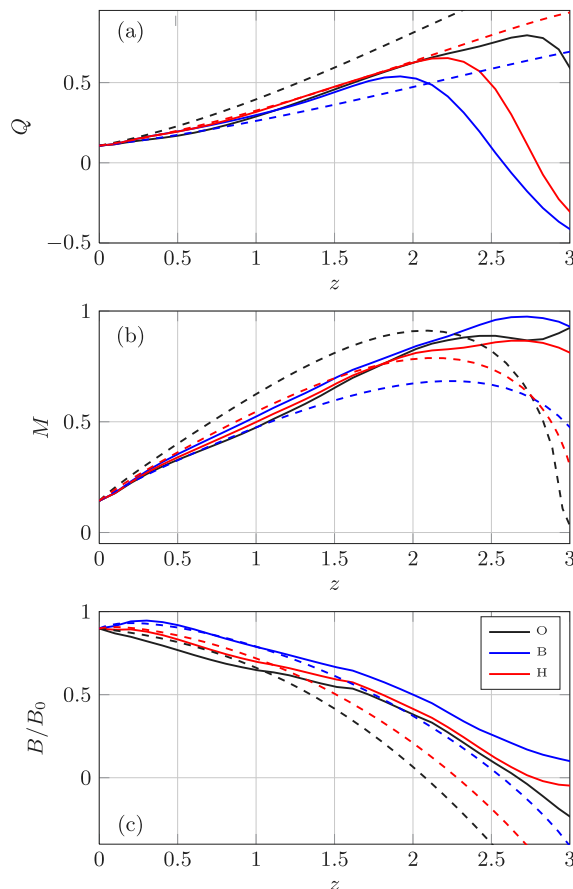


FIG. 12. (a) Volume flux Q for cases O, B, and H (solid) and integral model solution in Eq. (38)-(42) (dashed). (b) Momentum flux M . (c) Total normalized buoyancy flux B/B_0 .

Solution of the integral model given by Eqs. (38)-(42) requires information on the entrainment coefficient, α , the momentum amplification factor, γ , and the individual plume width ratios, λ_i . For demonstration purposes, we chose available values of the entrainment coefficient ranging from $\alpha = 0.093^8$ for the single-phase case to 0.055 for the pure bubble case.^{17,26} Corresponding values of the momentum amplification factor values are set to $\gamma_M = 1.1$ and 1.2 and the scalar-to-momentum plume widths ratios are $\lambda_o = 1.1$, $\lambda_T = 1.1$, and $\lambda_b = 0.8$. For the hybrid case, the values of entrainment coefficient and momentum amplification factor are the average between the two pure cases. Integral model results for the individual fluxes in each are shown by dashed lines in Fig. 12.

Given the close agreement between the values of Q and M computed from the full model simulation for all three cases and the integral model results for the volume flux, the best fit value of α corresponds to the hybrid plume case, $\alpha = 0.074$. For comparison, direct estimates from the full simulations for $\alpha = (dQ/dz)/(8\pi M)^{1/2}$ give values 0.079, 0.077, and 0.068 for cases O, H, and B, respectively. Similar estimates of $\gamma_M = (2BQ)/(dM^2/dz)$ over $0 < z < 1.5$ give 1.17 for case O and 1.30 for cases B and H. Despite differences in parameterization, the integral model formulation, explicitly accounting for the gas-phase slip velocity, reproduces the initial rise in buoyancy flux observed in both the pure bubble and hybrid plumes.

In addition to allowing best-fit parameter estimations, the full model simulations provide a means of checking basic assumptions in the integral model formulation. Beyond the primary entrainment assumption used to close the volume flux equation, the integral model derivation requires assumptions about (i) the self-similar shape of the vertical velocity and buoyancy fields and (ii) neglecting vertical turbulent transport terms in the evolution of the momentum and individual

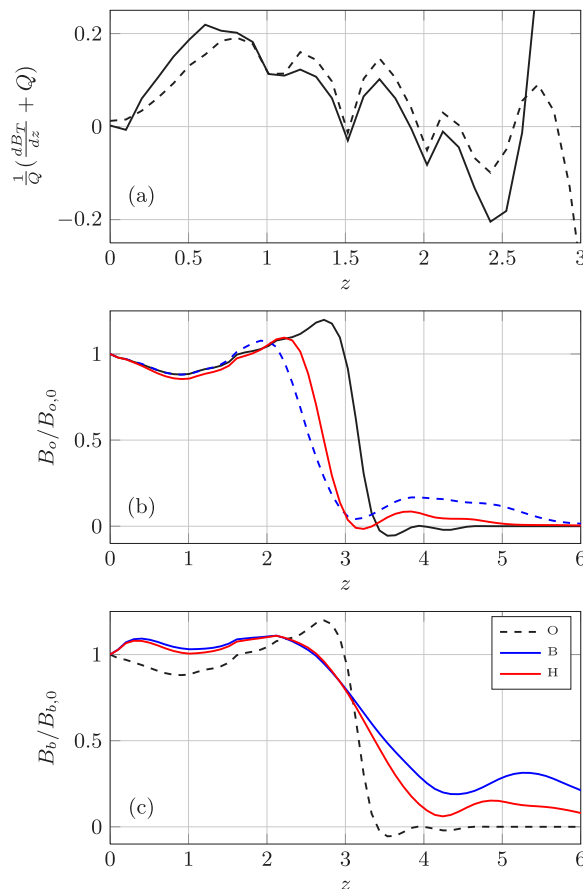


FIG. 13. (a) $dB_T/dz + Q$ (solid) and $-2\pi(d/dz)\int_0^\infty \langle w'\theta' \rangle r dr$ (dashed) weighted by Q for case O. (b) Buoyancy flux contribution from β , B_o , normalized by the inlet value. Dashed lines correspond to the flux of the passive scalar in each case. (c) Buoyancy flux contribution from gas volume fraction, B_b , normalized by the inlet value for cases O, B, and H.

buoyancy flux contributions. In the single phase case, the total buoyancy flux evolution for stably stratified environments,

$$\frac{dB}{dz} = \frac{dB_T}{dz} = -Q,$$

is exact in the absence of vertical turbulent fluxes.

Direct computation of the validity of the assumption is shown for the single-phase plume in the top panel of Fig. 13 where the error given by $dB_T/dz + Q$ (solid) is found to be substantial, 20% of Q itself at $z = 0.5$. For consistency, the direct computation of the vertical turbulence flux $-2\pi(d/dz) \int_0^\infty \langle w'\theta' \rangle r dr$ weighted by Q (dashed) is also shown. Figs. 13(b) and 13(c) indicate that similar results hold for the individual buoyancy flux contributions in all three cases. For example, neglecting turbulent transport implies that buoyancy flux contributions from the active scalar β , whose vertical flux is unaffected by thermal stratification, are constant in z . Instead, the computed flux decays initially where $\frac{d}{dz} \int_0^\infty \langle \beta'w' \rangle r dr > 0$ and then increases for $z \approx 1$ where the mean vertical velocity is maximal.

V. CONCLUSIONS

Multiphase turbulent buoyant plumes set by different inlet forcing due to the presence of gas and/or oil phases are considered. A comparison of the dynamics of three plumes with identical inlet buoyancy flux but different buoyancy sources, namely, a pure bubble, a pure oil, and a hybrid case, is presented.

Three vertical length scales have been used to characterize the plumes in stratified environments, namely, the location where the mean axial buoyancy vanishes z_{eq} , the location where the mean axial velocity vanishes or reaches its first minimum z_{max} and the location where the far-field scalar concentration peaks z_{th} . Results reveal that, as expected, the larger the amount of gas in the plume, the further z_{eq} and z_{max} are vertically shifted with respect to the single phase case. However, as the amount of bubbles increases, the location of the main lateral intrusion z_{th} decreases. The opposite trend of on-axis (z_{eq} and z_{max}) and far-field (z_{th}) characteristic heights on the inlet gas volume fraction is due to the significant changes in the downdraft velocity regions produced by the presence of a slipping gas phase. These changes significantly modify the turbulent mixing within the plume resulting in a reduction in the height of the inertial overshoot region ($z_{max} - z_{th}$) and an increase in the thickness of the primary lateral intrusion of liquid phase effluent in both pure gas and hybrid gas-“oil” plumes.

Rough comparisons can be made between the present numerical experiments, where the total buoyancy flux is held constant and the gas contribution varied, and pure gas bubble plume experiments for varying slip velocities.²³ Experimental results indicate that the trapping height, z_{th} , is relatively independent of the non-dimensional slip velocity for $U_N \lesssim 2$ but decreases with increasing U_N . On the other hand, the peeling height h_P (comparable to z_{max}) initially grows with U_N , reaches a maximum at $U_N \approx 2$, and then decays. This behavior is explained by the intensification of the downdrafts as the bubbles slip faster for $U_N \lesssim 2$. Eventually for larger values of slip velocity, the bubbly core is too narrow and loses its ability to support the plume resulting in a decay in h_P . The values of z_{th} and z_{max} for the current bubble plume compare well with the average values of trapping and peeling heights (shown in parenthesis in Table III) reported by Socolofsky and Adams²³ for the experiments at $U_N < 0.8$. Other quantities typically reported in double plume model studies are the fraction of tracer peeled for the first intrusion f^* and the non-dimensional first lateral intrusion flux $Q_{th} \equiv Q_i/(B^3N^{-5})^{1/4}$. The current work values shown in Table IV also compare well with those reported by Socolofsky and Adams.²³ While the fraction of the injected dye in the hybrid plume is closer to that found in the oil plume ($f^* = 1$), the main lateral intrusion volume flux is similar to that for the pure bubble case. The values of z_{th} , z_{eq} , f^* , and Q_{th} for the hybrid case more closely match those of the pure bubble case than the single-phase plume.

For fixed input buoyancy flux, standard plume metrics (characteristic vertical scales, peeling fraction of injected dye, and lateral intrusion volume flux) do not appear to vary linearly with the inlet gas volume fraction. Model results show that the hybrid plume, with only 50% of the inlet

TABLE IV. Fraction of tracer peeled f^* and non-dimensional first lateral intrusion flux Q_{th} .

Case	f^*	Q_{th}
O	1.0	0.47
H	0.96	0.55
B	0.88	0.60

bouyancy carried by the gas phase, is significantly closer to the pure bubble plume than to the single phase case. Relatively small values of gas volume fraction may lead to significant changes in the dynamics and overall shape of the plume.

Following standard approaches, closed equations for radially integrated volume, momentum, and buoyancy fluxes have been derived from the governing model set. The resulting integral equations directly account for gas-phase slip velocity via the same self-similarity arguments typically employed to close the momentum flux balance. Direct comparisons of the integral model solutions with the full simulations show general agreement for all cases using typical values of the model input parameters. In particular, the modified integral model reproduces the initial overshoot in gas-phase buoyancy flux produced by the slip-velocity. The comparisons also indicate that primary errors are introduced in the integral formulation by neglecting vertical turbulent transport terms in the evolution of individual buoyancy flux contributions.

Using the average values of inlet buoyancy flux $B_0 = 0.73 \text{ m}^4 \text{ s}^{-3}$ and buoyancy frequency $N = 0.0015 \text{ s}^{-1}$ for the Deepwater Horizon accident reported by Socolofsky *et al.*,³² the estimated location of the trapping height for a 50% hybrid plume, $z_{th} = 315 \text{ m}$, is in excellent agreement with fluorescence field measurements related to the concentration of dissolved and dispersed hydrocarbons.

ACKNOWLEDGMENTS

This research is supported by a grant from BP/The Gulf of Mexico Research Initiative. Additional computer resources have also been provided by City University of New York High Performance Computing Center under NSF Grant Nos. CNS-0855217, CNS-0958379, and ACI-1126113.

NOMENCLATURE

Symbol	Description
\mathbf{u}	Velocity vector
N	Buoyancy frequency
T	Temperature
α	Entrainment coefficient
α_k	Volume fraction of phase k
β	Volume fraction of buoyancy-active scalar
ρ	Density
γ	Thermal expansion coefficient
ζ	Relative density ratio
ζ	Background stratification slope
γ_M	Momentum amplification factor
λ	Scalar to momentum plume width ratio
θ	Temperature perturbation
ξ	Relative thermal expansion coefficient difference
Superscripts and subscripts	Description
l	Liquid phase

b	Gas phase
m	Mixture
s	Slip velocity
w	Water
e	Environment

- ¹ R. Camilli, C. M. Reddy, D. R. Yoerger, B. A. S. Van Mooy, M. V. Jakuba, J. C. Kinsey, C. P. McIntyre, S. P. Sylva, and J. V. Maloney, "Tracking hydrocarbon plume transport and biodegradation at Deepwater Horizon," *Science* **330**, 201–204 (2010).
- ² M. McNutt, R. Camilli, G. Guthrie, P. Hsieh, V. Labson, B. Lehr, D. Maclay, A. Ratzel, and M. Sogge, "Assessment of flow rate estimates for the Deepwater Horizon/Macondo well oil spill," Technical Report, Flow Rate Technical Group report to the National Incident Command, Interagency Solutions Group, 2011; available at http://large.stanford.edu/courses/2011/ph240/minal/docs/FRTG-final-report3_10_11-final-pdf.pdf.
- ³ W. Schmidt, "Turbulent propagation of a stream of heated air," *Z. Angew. Math. Mech.* **21**, 265–351 (1941).
- ⁴ Y. B. Zeldovich, "Limiting laws for turbulent flows in free convection," *Zh. Eksp. Teor. Fiz.* **7**, 1463–1465 (1937).
- ⁵ H. Tennekes and J. L. Lumley, *A First Course in Turbulence* (MIT Press, 1972).
- ⁶ A. Shabbir and W. K. George, "Experiments on a round turbulent buoyant plume," *J. Fluid Mech.* **275**, 1–32 (1994).
- ⁷ G. I. Taylor, "Dynamics of a mass of hot gas rising in air," Technical Report MDDC 919, LADC 276, US Atomic Energy Commission, 1945.
- ⁸ B. R. Morton, G. Taylor, and J. S. Turner, "Turbulent gravitational convection from maintained and instantaneous sources," *Proc. R. Soc. London, Ser. A* **24**, 1–23 (1956).
- ⁹ B. J. Devenish, G. G. Rooney, and D. J. Thomson, "Large-eddy simulations of a buoyant plume in uniform and stably stratified environments," *J. Fluid Mech.* **652**, 75–103 (2010).
- ¹⁰ L. J. Bloomfield and R. C. Kerr, "A theoretical model of a turbulent fountain," *J. Fluid Mech.* **424**, 197–216 (2000).
- ¹¹ T. J. McDougall, "Bubble plumes in stratified environments," *J. Fluid Mech.* **85**, 655–672 (1978).
- ¹² T. L. Norman and S. T. Revankar, "Buoyant jet and two-phase jet-plume modeling for application to large water pools," *Nucl. Eng. Des.* **241**, 1667–1700 (2011).
- ¹³ I. E. Lima Neto, "Modelling the liquid volume flux in bubbly jets using a simple integral approach," *J. Hydraulic Eng.* **138**, 210–215 (2012).
- ¹⁴ E. Kaminski, S. Tait, and G. Carazzo, "Turbulent entrainment in jets with arbitrary buoyancy," *J. Fluid Mech.* **526**, 361–376 (2005).
- ¹⁵ G. Carazzo, E. Kaminski, and S. Tait, "The route to self-similarity in turbulent jets and plumes," *J. Fluid Mech.* **547**, 137–148 (2006).
- ¹⁶ D. T. Conroy and S. G. L. Smith, "Endothermic and exothermic chemically reacting plumes," *J. Fluid Mech.* **612**, 291–310 (2008).
- ¹⁷ T. Asaeda and J. Imberger, "Structure of bubble plumes in linearly stratified environments," *J. Fluid Mech.* **249**, 35–57 (1993).
- ¹⁸ J. D. Dittmars and K. Cederwall, "Analysis of air-bubble plumes," in *Coastal Engineering* (American Society of Civil Engineers, 1974), Chap. 128, pp. 2209–2226.
- ¹⁹ S. S. S. Cardoso and S. T. McHugh, "Turbulent plumes with heterogeneous chemical reaction on the surface of small buoyant droplets," *J. Fluid Mech.* **642**, 49–77 (2009).
- ²⁰ A. Fabregat, W. K. Dewar, T. M. Özgökmen, A. C. Poje, and N. Wienders, "Numerical simulations of turbulent thermal, bubble and hybrid plumes," *Ocean Modell.* **90**, 16–28 (2015).
- ²¹ J. H. Milgram, "Mean flow in round bubble plumes," *J. Fluid Mech.* **133**, 345–376 (1983).
- ²² S. A. Socolofsky and E. E. Adams, "Liquid volume fluxes in stratified multiphase plumes," *J. Hydraulic Eng.* **129**, 905–914 (2003).
- ²³ S. A. Socolofsky and E. E. Adams, "Role of slip velocity in the behavior of stratified multiphase plumes," *J. Hydraulic Eng.* **131**, 273–282 (2005).
- ²⁴ T. J. McDougall, "Negatively buoyant vertical jets," *Tellus* **33**, 313–320 (1981).
- ²⁵ C. R. Liro, E. E. Adams, and H. J. Herzog, "Modelling the release of CO₂ in the deep ocean," *Energy Convers. Manage.* **33**, 667–674 (1992).
- ²⁶ S. A. Socolofsky, T. Bhaumik, and D. G. Seol, "Double-plume integral models for near-field mixing in multiphase plumes," *J. Hydraulic Eng.* **134**, 772–783 (2008).
- ²⁷ A. K. Chesters, M. van Doorn, and L. H. J. Goossens, "A general model for unconfined bubble plumes from extended sources," *Int. J. Multiphase Flow* **6**, 499–521 (1980).
- ²⁸ A. M. Leitch and W. D. Baines, "Liquid volume flux in a weak bubble plume," *J. Fluid Mech.* **205**, 77–98 (1989).
- ²⁹ P. G. Baines, "Two-dimensional plumes in stratified environments," *J. Fluid Mech.* **471**, 315–337 (2002).
- ³⁰ A. Wüest, N. H. Brooks, and D. M. Imboden, "Bubble plume modelling for lake restoration," *Water Resour. Res.* **28**, 3235–3250, doi:10.1029/92WR01681 (1992).
- ³¹ C. J. Lemckert and J. Imberger, "Energetic bubble plumes in arbitrary stratification," *J. Hydraulic Eng.* **119**, 680–703 (1993).
- ³² S. A. Socolofsky, E. E. Adams, and C. R. Sherwood, "Formation dynamics of subsurface hydrocarbon intrusions following the deepwater horizon blowout," *Geophys. Res. Lett.* **38**, L09602, doi:10.1029/2011GL047174 (2011).
- ³³ A. Sokolichin, G. Eigenberger, and A. Lapin, "Simulation of buoyancy driven bubbly flow: Established simplifications and open questions," *AIChE J.* **50**(1), 24–45 (2004).
- ³⁴ M. T. Dhotre, B. Niceno, B. L. Smith, and M. Simiano, "Large-eddy simulation (LES) of the large scale bubble plume," *Chem. Eng. Sci.* **64**, 2692–2704 (2009).
- ³⁵ D. A. Drew, "Mathematical modelling of two-phase flow," *Annu. Rev. Fluid Mech.* **15**, 261–291 (1983).

- ³⁶ G. C. Buscaglia, F. A. Bombardelli, and M. H. Garca, “Numerical modeling of large-scale bubble plumes accounting for mass transfer effects,” *Int. J. Multiphase Flow* **28**, 1763–1785 (2002).
- ³⁷ O. Simonin and P. L. Viollet, “Modeling of turbulent two-phase jets loaded with discrete particles,” in *Phase-Interface Phenomena in Multiphase Flows* (Hemisphere Publishing Corporation, 1990), pp. 259–269.
- ³⁸ M. Simiano, “Experimental investigation of large-scale three dimensional bubble plume dynamics,” Ph.D. thesis, Swiss Federal Institute of Technology Zurich, 2005.
- ³⁹ D. A. Drew and S. L. Passman, *Theory of Multicomponent Fluids* (Springer-Verlag, 1999), Vol. 135.
- ⁴⁰ G. H. Jirka, “Integral model for turbulent buoyant jets in unbounded stratified flows. Part I: Single round jet,” *Environ. Fluid Mech.* **4**, 1–56 (2004).
- ⁴¹ H. Wang and A. W.-K. Law, “Second-order integral model for a round turbulent buoyant jet,” *J. Fluid Mech.* **459**, 397–428 (2002).
- ⁴² A. Ezzamel, P. Salizzoni, and G. R. Hunt, “Dynamical variability of axisymmetric buoyant plumes,” *J. Fluid Mech.* **765**, 576–611 (2015).
- ⁴³ M. G. Domingos and S. S. S. Cardoso, “Turbulent two-phase plumes with bubble-size reduction owing to dissolution or chemical reduction,” *J. Fluid Mech.* **716**, 120–136 (2013).
- ⁴⁴ B. R. Morton, “Forced plumes,” *J. Fluid Mech.* **5**, 151–163 (1959).
- ⁴⁵ G. R. Hunt and N. G. Kaye, “Virtual origin correction for lazy turbulent plumes,” *J. Fluid Mech.* **435**, 377–396 (2001).
- ⁴⁶ E. Applequist and P. Schlatter, “Simulating the Laminar von Kármán flow in nek5000,” Technical Report diva2:722144, KTH Mechanics, 2014.
- ⁴⁷ A. Fabregat Tomàs, A. C. Poje, T. M. Özgökmen, and W. K. Dewar, “Effects of rotation on turbulent buoyant plumes in stratified environments,” *J. Geophys. Res., Oceans* **121**, 5397–5417, doi:10.1002/2016JC011737 (2016).
- ⁴⁸ M. V. Pham, F. Plourde, and S. Doan-Kim, “Direct and large-eddy simulations of a pure thermal plume,” *Phys. Fluids* **19**, 125103 (2007).
- ⁴⁹ F. Plourde, M. V. Pham, S. Doan-Kim, and S. Balachandar, “Direct numerical simulation of a rapidly expanding thermal plume: Structure and entrainment interaction,” *J. Fluid Mech.* **604**, 99–123 (2008).
- ⁵⁰ P. F. Fischer, J. W. Lottes, and S. G. Kerkemeier, Nek5000 web page, <http://nek5000.mcs.anl.gov>, 2008.
- ⁵¹ M. O. Deville, P. F. Fischer, and E. H. Mund, *High-Order Methods for Incompressible Fluid Flow* (Cambridge University Press, 2002).
- ⁵² T. M. Özgökmen, T. Iliescu, and P. F. Fischer, “Large eddy simulation of stratified mixing in a three-dimensional lock-exchange system,” *Ocean Modell.* **26**, 134–155 (2009).
- ⁵³ T. M. Özgökmen, T. Iliescu, and P. F. Fischer, “Reynolds number dependence of mixing in a lock-exchange system from direct numerical and large eddy simulations,” *Ocean Modell.* **30**, 190–206 (2009).
- ⁵⁴ G.-S. Karamanos and G. E. Karniadakis, “A spectral vanishing viscosity method for large-eddy simulations,” *J. Comput. Phys.* **163**, 22–50 (2000).
- ⁵⁵ P. F. Fischer and J. S. Mullen, “Filter-based stabilization of spectral element methods,” *C. R. Acad. Sci.-Ser. I-Math.* **332**, 265–270 (2001).
- ⁵⁶ K. Koal, J. Stiller, and H. M. Blackburn, “Adapting the spectral vanishing viscosity method for large-eddy simulations in cylindrical configurations,” *J. Comput. Phys.* **231**, 3389–3405 (2012).
- ⁵⁷ T. S. Richards, Q. Aubourg, and B. R. Sutherland, “Radial intrusions from turbulent plumes in uniform stratification,” *Phys. Fluids* **26**, 036602-1–036602-17 (2014).
- ⁵⁸ T. V. Crawford and A. S. Leonard, “Observations of buoyant plumes in calm stably stratified air,” *J. Appl. Meteorol.* **1**, 251–256 (1962).
- ⁵⁹ A. B. Tsinober, Y. Yahalom, and D. J. Shlien, “A point source of heat in a stable salinity gradient,” *J. Fluid Mech.* **135**, 199–217 (1983).